Monthly Notices
of the
ROYAL ASTRONOMICAL SOCIETY

MNRAS **458,** 1939–1947 (2016)
Advance Access publication 2016 March 7

doi:10.1093/mnras/stw384

Relativistic tearing and drift-kink instabilities in two-fluid simulations

Maxim V. Barkov[1]★ and Serguei S. Komissarov[2]★

[1]*Astrophysical Big Bang Laboratory, RIKEN, 351-0198 Saitama, Japan*
[2]*Department of Applied Mathematics, The University of Leeds, Leeds, LS2 9JT*

Accepted 2016 February 16. Received 2016 February 16; in original form 2015 July 16

ABSTRACT

The stability of current sheets in collisionless relativistic pair plasma was studied via two-dimensional two-fluid relativistic magnetohydrodynamic simulations with vanishing internal friction between fluids. In particular, we investigated the linear growth of the tearing and drift-kink modes in the current sheets both with and without the guide field and obtained the growth rates which are very similar to what has been found in the corresponding particle in cell (PIC) simulations. This suggests that the two-fluid simulations can be useful in studying the large-scale dynamics of astrophysical relativistic plasmas in problems involving magnetic reconnection.

Key words: magnetic fields – MHD – plasmas – relativistic processes – waves – methods: numerical.

1 INTRODUCTION

It is now well recognized that magnetic field is a 'major player' in the dynamics of astrophysical plasma – the Lorentz force shapes a wide variety of flows in the Universe. The dissipative effects are also important, leading to magnetic reconnection and explosive release of stored magnetic energy. This could be of particular relevance in the astrophysics of neutron stars and black holes, which are expected to produce relativistic magnetically dominated plasma. Magnetic reconnection accompanied by dissipation of magnetic energy may be the main processes leading to the observed non-thermal emission from winds and jets produced by these compact relativistic objects (e.g. Romanova & Lovelace 1992; Drenkhahn & Spruit 2002; Lyutikov & Blandford 2003; Zhang & Yan 2011; McKinney & Uzdensky 2012; Komissarov 2013; Porth, Komissarov & Keppens 2013, 2014).

The magnetic dissipation associated with the magnetic reconnection is not captured in the framework of ideal relativistic magnetohydrodynamic (MHD), which is currently the most common tool of modelling astrophysical phenomena. The approximation of resistive MHD does introduce Ohmic dissipation of magnetic field but the astrophysical plasmas are often collisionless, whereas the resistivity has strong physical justification only for collisional plasmas.

Kinetic models of plasma are better routed in fundamental physics and more suitable for collisionless plasma but they are also much more complex and computationally expensive. PIC-simulations, based on dynamics of individual particles (or rather 'superparticles'), are also quite expensive. Studies based on these methods shows that fast magnetic reconnection involves development of current sheets whose thickness is comparable to the electron skin depth, the kinetic scale absent in single fluid MHD (Zenitani & Hoshino 2001, 2007; Bessho & Bhattacharjee 2012; Cerutti et al. 2014; Sironi & Spitkovsky 2014; Liu et al. 2015).

Half-way between these frameworks and the single fluid MHD are the multifluid models, where plasma is considered as a collection of several interpenetrating charged and neutral fluids, coupled via macroscopic electromagnetic field. Like a single fluid MHD, this approach is well suited for studying the large-scale dynamics of plasma flows. Moreover, it also captures some elements of plasma microphysics in the form of collective interaction between its positively and negatively charged components, which leads to the emergence of the plasma frequency and electron skin depth. Its generalized Ohm's law has several terms which introduce non-ideal properties even in the absence of explicit internal friction between fluids. For this reason, the multifluid approximation is considered as a potential alternative to more expensive kinetic and PIC approaches when it comes to problems of macroscopic plasma dynamics where the magnetic reconnection plays an important dynamic role via restructuring of magnetic field and magnetic dissipation. For relativistic plasma, created in magnetospheres of neutron stars and black holes via various pair production processes, a simple two-fluid approximation involving electron and positron fluids may be sufficient. Obviously, the lack of spectral information means that the fluid framework has rather limited potential for addressing such important issues as radiation and non-thermal particle acceleration.

So far, there has been only a rather limited effort to explore the potential of the two-fluid approximation in numerical modelling of relativistic plasma. Zenitani, Hesse & Klimas (2009a,b) used this approach for studying the relativistic magnetic reconnection, Amano & Kirk (2013) to study the termination shocks of pulsar winds, and Kojima & Oogi (2009) tried to construct two-fluid models of steady-state pulsar magnetospheres. In the same

★E-mail: barmv05@gmail.com (MVB); S.S.Komissarov@leeds.ac.uk (SSK)

way as this is done in resistive MHD simulations, Zenitani et al. (2009a,b) used anomalous resistivity to trigger fast magnetic reconnection of Petschek-type. However, they noticed that the inertial terms of the generalized Ohm's law also make a significant contribution to the reconnection electric field, even exceeding that of the friction term, which represents the resistivity. Based on this observation, they suggested that the inertial terms alone may be sufficient to sustain magnetic reconnection. The robustness of this conclusion is not clear as they have also found that the simulations outcome strongly depends on the model of resistivity. Moreover, they used the Lax–Wendroff numerical scheme which also introduces numerical resistivity, whose contribution to the reconnecting electric field exceeds the other terms (Zenitani et al. 2009a,b). However, if the two-fluid model can reproduce the reconnection rate sufficiently accurately then this approach becomes very useful for studying large-scale phenomena where magnetic restructuring and dissipation are important dynamical factors.

Until recently, the fast magnetic reconnection was viewed in the context of the Petschek model with its compact diffusion zone, as opposed to the slow Sweet–Parker type reconnection of long and thin current sheets. However, long current sheets are unstable to tearing mode instability (TI), which splits it into much shorter current sheets separated by plasmoids. Two-dimensional (2D) simulations discovered that at the non-linear stage the current sheet becomes highly dynamic, with mergers of original plasmoids and creation of new ones. This leads to a much higher overall reconnection rate (e.g. Biskamp 1986; Shibata & Tanuma 2001; Loureiro, Schekochihin & Cowley 2007; Bhattacharjee et al. 2009; Uzdensky, Loureiro & Schekochihin 2010). In addition to TI, currents sheets are also subject to the so-called drift-kink instability (DKI) which grows faster (Zenitani & Hoshino 2007; Cerutti et al. 2014). This discovery suggested that DKI may hinder the development of TI. However, recent 3D PIC simulations, where both types of modes are allowed, show that TI is not suppressed and becomes dominant at the non-linear phase. The reconnection rates in 3D and 2D simulations are found to be similar (Sironi & Spitkovsky 2014; Liu et al. 2015).

Given the importance of TI and DKIs in the fast magnetic reconnection, the potential of the two-fluid model depends on how well it can describe their development. In this paper, we focus on the linear development of these instabilities numerically. To this aim, we used our recently developed two-fluid code for pair plasma (JANUS; Barkov et al. 2014). This code is based on a Godunov-type numerical scheme which is much less dissipative compared to the Lax–Wendroff one. It is third-order accurate in smooth regions, which makes it powerful tool for studying the instabilities. By setting the internal friction between the fluids (the resistivity) to zero we focus on the role of the inertial terms in the generalized Ohm's law. The results are compared with the growth rates obtained via PIC simulations by other groups. In the follow-up paper, we will discuss the non-linear phases of magnetic reconnection in the plasmoid-dominated regime.

2 TWO-FLUID MODEL OF PAIR PLASMA

Following Zenitani et al. (2009b), we adopt the 3+1 (−+++) Special Relativistic equations originated from the covariant formulation by Gurovich & Solov'ev (1986). The corresponding dimensionless equations are (for details see Barkov et al. 2014)

(i) the continuity equations

$$\partial_t(n_\pm\gamma_\pm) + \nabla_i(n_\pm u^i_\pm) = 0\,; \tag{1}$$

(ii) the total energy equation

$$\partial_t\left(\sum_\pm(w_\pm\gamma_\pm^2 - p_\pm) + \frac{\mathcal{K}_\mathrm{q}}{2\mathcal{K}_\mathrm{m}}(B^2+E^2)\right) + \nabla_i\left(\sum_\pm w_\pm\gamma_\pm u^i_\pm + \frac{\mathcal{K}_\mathrm{q}}{\mathcal{K}_\mathrm{m}}e^{ijk}E_jB_k\right) = 0\,; \tag{2}$$

(iii) the total momentum equation

$$\partial_t\left(\sum_\pm w_\pm\gamma_\pm u^s_\pm + \frac{\mathcal{K}_\mathrm{q}}{\mathcal{K}_\mathrm{m}}e^{sjk}E_jB_k\right) + \nabla_i\left(\sum_\pm(w_\pm u^i_\pm u^s_\pm + p_\pm g^{is}) + \frac{\mathcal{K}_\mathrm{q}}{\mathcal{K}_\mathrm{m}}\left(-E^iE^s - B^iB^s + \frac{1}{2}(B^2+E^2)g^{is}\right)\right) = 0\,; \tag{3}$$

(iv) the Maxwell equations

$$\nabla_iB^i = 0\,, \tag{4}$$

$$\partial_tB^s + e^{sik}\partial_iE_k = 0\,, \tag{5}$$

$$\nabla_iE^i = \frac{1}{\mathcal{K}_\mathrm{q}}(n_+\gamma_+ - n_-\gamma_-)\,, \tag{6}$$

$$\partial_tE^s - e^{sik}\partial_iB_k = -\frac{1}{\mathcal{K}_\mathrm{q}}(n_+u^s_+ - n_-u^s_-)\,. \tag{7}$$

(v) and the generalized Ohm's law

$$\partial_t\left(\sum_\pm\pm w_\pm\gamma_\pm u^s_\pm\right) + \nabla_i\left(\sum_\pm\pm(w_\pm u^i_\pm u^s + p_\pm g^{is})\right) = \frac{1}{\mathcal{K}_\mathrm{m}}\tilde{n}(E^s + e^{sik}v_iB_k) + \frac{2}{\mathcal{K}_\mathrm{f}}n_+n_-(u^s_- - u^s_+)\,. \tag{8}$$

In these equations E and B are the electric and magnetic field, $n_\pm$, $p_\pm$, $w_\pm$, $\gamma_\pm$ and $u_\pm = \gamma_\pm v_\pm$ are the density, pressure, relativistic enthalpy, Lorentz factor and four-velocity of electron and positron fluids, respectively, g^{ik} is the spatial metric tensor of Minkowski space–time and, e^{ijk} is the Levi–Civita tensor, indexes s, i and k correspond to three spatial direction.

In the Ohm's law, $\tilde{n} = n_+\gamma_+ + n_-\gamma_-$ is the total number density of charged particles as measured in the laboratory frame and $v^i = (n_+\gamma_+v^i_+ + n_-\gamma_-v^i_-)/\tilde{n}$ is their average velocity in this frame. The last term of the Ohm's law describes the internal friction between the fluids, which is related to resistivity.

The three dimensionless parameters in these equations are

$$\mathcal{K}_\mathrm{q} = \frac{B_0}{4\pi eL_0n_0}\,,\quad \mathcal{K}_\mathrm{m} = \frac{m_\mathrm{e}c^2}{eB_0L_0}\,,\quad \mathcal{K}_\mathrm{f} = \frac{m_\mathrm{e}c}{\varkappa_\mathrm{f}n_0L_0}\,, \tag{9}$$

where L_0 is the characteristic length-scale, the speed of light, c, is the characteristic speed, B_0 the characteristic value of magnetic (and electric) field, n_0 the characteristic number density of particles and e is the electron charge. The corresponding scales for the time is $T_0 = L_0/c$, for the mass density $m_\mathrm{e}n_0$ and for the pressure and enthalpy $m_\mathrm{e}c^2n_0$, $\varkappa_\mathrm{f}$ is the dynamic coefficient of friction between these fluids.

The dimensionless polytropic equation of state (EOS) is

$$w_{\pm} = n_{\pm} + \Gamma p_{\pm}/(\Gamma - 1)\,, \tag{10}$$

where Γ is the ratio of specific heats.

In this paper, we solve these equations numerically, using the code JANUS (Barkov et al. 2014). The code is based on a conservative finite-difference scheme which utilizes a third-order WENO interpolation (Liu, Osher & Chan 1994; Yamaleev & Carpenter 2009) and a third-order TVD time integration of the Runge–Kutta type (Shu & Osher 1988), thus ensuring overall third-order accuracy on smooth solutions. Hyperbolic fluxes are computed using the Lax–Friedrich prescription. The magnetic field is kept near divergence-free by means of the method of generalized Lagrange multiplier (Munz et al. 2000; Dedner et al. 2002; Komissarov 2007).

3 HARRIS CURRENT SHEET

In this paper, we study stability of the Harris current sheet using Cartesian coordinates aligned with the sheet. In these coordinates, the initial magnetic field $\boldsymbol{B} = (B_x(y), 0, B_z)$, where B_z is a uniform guide field and

$$B_x = B_\infty \tanh\left(\frac{y}{\delta}\right)\,, \tag{11}$$

where δ is the half-thickness of the current sheet and B_∞ is the magnetic field strength far away from the sheet. The force equilibrium of the current sheet implies the total gas pressure distribution

$$p_t = p_\infty + \frac{B_\infty^2}{8\pi}\left(1 - \tanh^2\left(\frac{y}{\delta}\right)\right)\,. \tag{12}$$

The gas pressure in the centre of the current sheet $p_0 = p_\infty + B_\infty^2/8\pi$. Introducing the pressure ratio $f_p = p_0/p_\infty$, we find that

$$f_p = 1 + \beta_m^{-1}, \tag{13}$$

where $\beta_m = 8\pi p_\infty/B_\infty^2$ is the traditional (non-relativistic) magnetization parameter of plasma. Following previous studies, we assume that the plasma temperature is uniform and hence the particle density distribution follows that of the gas pressure.

The half-thickness δ determines the drift speed of fluids in the current sheet. From the Faraday equation we find four velocity as

$$u_-^z = \frac{cB_\infty}{8\pi\delta e n_-}\mathrm{sech}^2\left(\frac{y}{\delta}\right)\,, \tag{14}$$

where we used the charge neutrality condition $n_- = n_+$, and hence $u_+ = -u_-$.

Using B_∞, δ and $n_\infty^\pm$ as the characteristic scales B_0, L_0 and n_0 of the problem, we find

$$\mathcal{K}_\mathrm{q} = 2u_0 f_p \quad \text{and} \quad \mathcal{K}_\mathrm{m} = \frac{1}{4\theta(f_p - 1)}\,, \tag{15}$$

where u_0 is the magnitude of u_-^z at the centre of the current sheet and $\theta = k_b T/m_e c^2$ is the dimensionless temperature, here k_b is Boltzmann constant. Following Cerutti et al. (2014), we use $f_p = 10$ and $u_0 = 0.75$ but set $\theta = 10$ instead of 10^8. The latter should not have a strong effect as in both cases the thermal energy dominates in the plasma inertia and this is indeed what has been found in the previous theoretical and numerical studies (Zelenyi & Krasnoselskikh 1979; Zenitani & Hoshino 2007). Given these values, we have $\mathcal{K}_\mathrm{q} = 15$ and $\mathcal{K}_\mathrm{m} = 0.042$. The corresponding relativistic magnetization parameter

$$\sigma_\infty = \frac{B_\infty^2}{4\pi w_\infty} \approx 4.4\,,$$

where $w_\infty = w_{-,\infty} + w_{+,\infty}$. Using the definitions of the plasma Larmor radius, $\rho_0 = \theta m_e c^2/eB_\infty$, and the skin depth, $d_e^2 = \theta m_e c^2/(4\pi n_\infty e^2)$, as in Cerutti et al. (2014), we find $\delta = 2.4\rho_0$ and $\delta = 1.26 d_e$, which is similar to what they have in the setup of their PIC simulations ($\delta = 2.7\rho_0$ and $\delta = 1.61 d_e$).[1]

4 SIMULATIONS

All simulations presented in this paper are 2D. We split them in four groups. In Sections 4.1 and 4.2, we present our studies of the tearing and DKIs of the Harris current sheet described in Section 3, without the guide field. The main goal is to obtain dispersion curves and compare them against the results of PIC simulations. In Section 4.3, we investigate the role of the guide field, by studying the response of modes with highest growth rates. In all models, the ratio of specific heats, $\Gamma = 4/3$ and Courant number C = 0.5. All physical parameters are dimensionalized using the characteristic scales c, $L_0 = \delta$, $B_0 = B_\infty$ and $n_0 = n_\infty$.

In order to focus on the role of inertial terms in Ohm's law, we effectively remove the resistive term by setting $\mathcal{K}_\mathrm{f} = 10^{15}$.

4.1 Tearing instability without guide field

For the study of the tearing instability, we consider a 2D problem with $\partial_z = 0$. The current sheet is pushed out of equilibrium by perturbing the magnetic field, $\boldsymbol{B} \to \boldsymbol{B} + \boldsymbol{b}$, where the divergence-free perturbation

$$\boldsymbol{b} = b_0 e^{-(y/l)^2}\left[-\frac{2y}{(kl^2)}\cos(kx)\boldsymbol{i}_x + \sin(kx)\boldsymbol{i}_y\right]\,, \tag{16}$$

where $k = 2\pi/\lambda$ is the wavenumber and $b_0 = 10^{-3}$ is the amplitude of the perturbation. In the x-direction, the size of the computational domain is set to be exactly one wavelength of the perturbation and we employ the periodic boundary conditions at the x boundaries. In the y-direction, we have a comparable size of the computational domain and use the free-flow boundary conditions. The basic parameters of the simulations are given in the Table 1.

To quantify the perturbation amplitude we use the maximum value of B^y in the computational domain. Fig. 1 shows examples of the amplitude evolution for a number of models. As the initial perturbation is not a normal mode of the instability, it leads to excitement not only of the normal mode with the wavelength equal to the x size of the computational box, the fundamental mode, but also its overtones as well as and propagating waves. The latter are partially transmitted through the y boundaries of the computational box and do not grow in amplitude. Soon they become dominated by the unstable normal modes. When the wavelength of the fundamental mode is below the maximum of the dispersion curve, it completely dominates the evolution as the parasitic overtones grow slower. This is illustrated in Fig. 2.

When the wavelength of the fundamental mode is above the maximum, the evolution is more complicated. Initially, it dominates overtones simply because its initial amplitudes is higher. However, some parasitic overtones may now grow faster and eventually overtake it while still at the linear phase. In the amplitude plots, this is manifested by an increase of the curve gradient, as exhibited by the curve of the TW160 model in Fig. 1. In the 2D plots of the solution,

[1] The difference is probably because they used $v_0 = \sqrt{0.6}$ and not $v_0 = 0.6$ as stated in their paper. We realized this issue a bit too late.

Table 1. TI models. The case without guide field. Here λ and ω_i are initial perturbation wavelength and perturbation grow rate, respectively.

Name	Resolution	domain X	domain Y	λ	ω_i
TW06	128 × 128	[−3,3]	[−5,5]	6	0.0
TW07	128 × 128	[−3.5,3.5]	[−5,5]	7	0.0
TW08	128 × 128	[−4,4]	[−5,5]	8	0.011
TW09	128 × 128	[−4.5,4.5]	[−5,5]	9	0.041
TW10	128 × 128	[−5,5]	[−5,5]	10	0.0603
TW11	128 × 128	[−5.5,5.5]	[−5,5]	11	0.077
TW12	160 × 128	[−6,6]	[−5,5]	12	0.085
TW14	160 × 160	[−7,7]	[−7,7]	14	0.095
TW20	256 × 256	[−10,10]	[−10,10]	20	0.100
TW30	384 × 256	[−15,15]	[−10,10]	30	0.089
TW40	512 × 256	[−20,20]	[−10,10]	40	0.079
TW80	1024 × 512	[−40,40]	[−20,20]	80	0.047
TW160	2048 × 1024	[−80,80]	[−40,40]	160	0.030
TW10h	192 × 192	[−5,5]	[−5,5]	10	0.0657
TW10H	256 × 256	[−5,5]	[−5,5]	10	0.0669

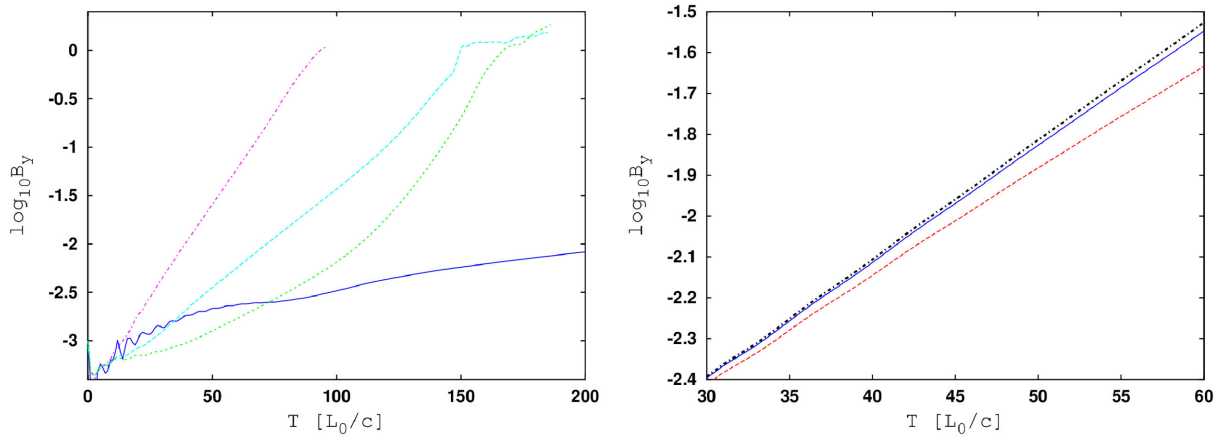

Figure 1. Left-hand panel: evolution of the perturbation amplitude for the models TW08 (blue solid line), TW30 (magenta dot–dashed line), TW80 (cyan dashed line) and TW160 (green dotted line). Right-hand panel: evolution of the perturbation amplitude for the models TW10 (solid line), TW10h (dashed line) and TW10H (dot–dashed line) which differ only by resolution.

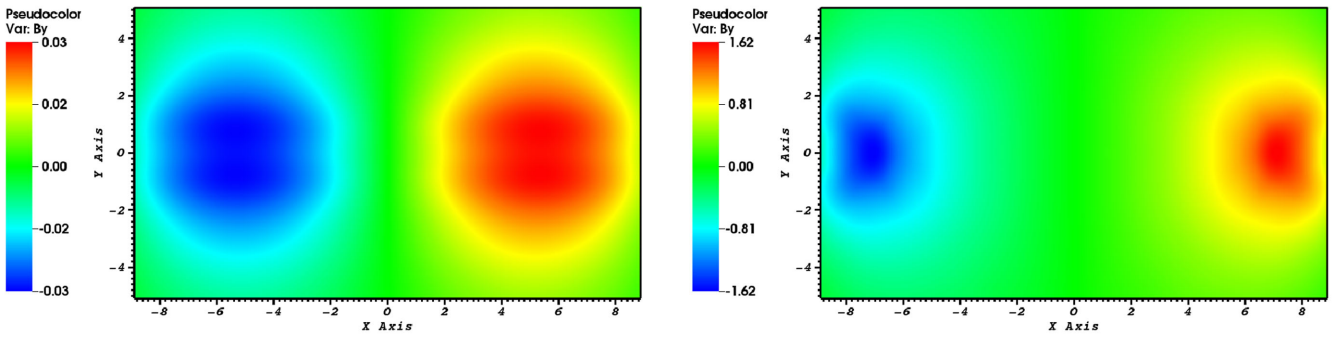

Figure 2. The distribution of B_y for the model TW20 at the times $t = 23$ (top panel) and $t = 88$ (bottom panel).

this is manifest by the appearance of dominant small scale structures (see Fig. 3). This has to be taken into account when measuring the growth rate of the fundamental mode.

We have checked the convergence of our numerical results by comparing the data obtained with different numerical resolutions. The right-hand panel of Fig. 1 shows the results for the model TW10 obtained with 128 × 128 cells, 192 × 192 cells (TW10h) and 256 × 256 (TW10H), which clearly indicate their convergence. Based on the study we conclude the numerical error of our growth rates does not exceed 10 per cent.

The growth rates, ω_i, of the fundamental modes are collected in Table 1 and Fig. 4. The results agree with the theoretical models which predict instability for $0 < k < 1$ with a peak at $k \approx 0.5$ (Zelenyi & Krasnoselskikh 1979; Pétri & Kirk 2007). The PIC

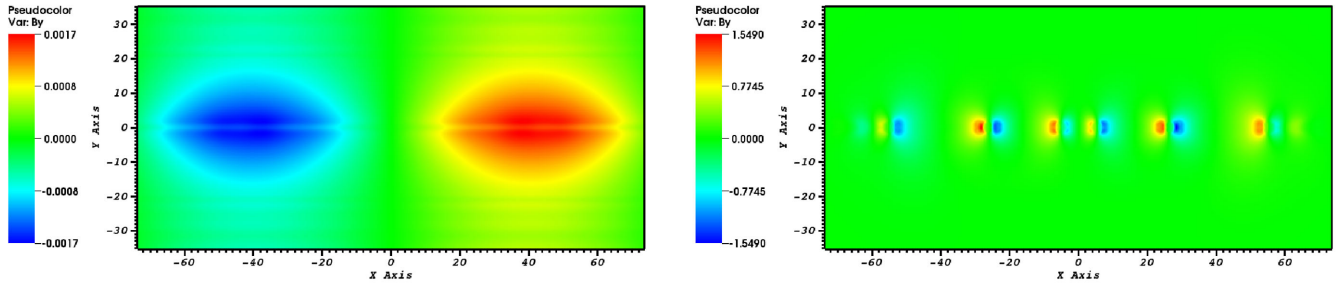

Figure 3. The distribution of B_y for the model TW160 at the times $t = 60$ (top panel) and $t = 180$ (bottom panel). One can see that initially it is the original perturbation of the wavelength equal to the domain length in the x-direction which dominates. However, at later times shorter wavelengths begin to dominate.

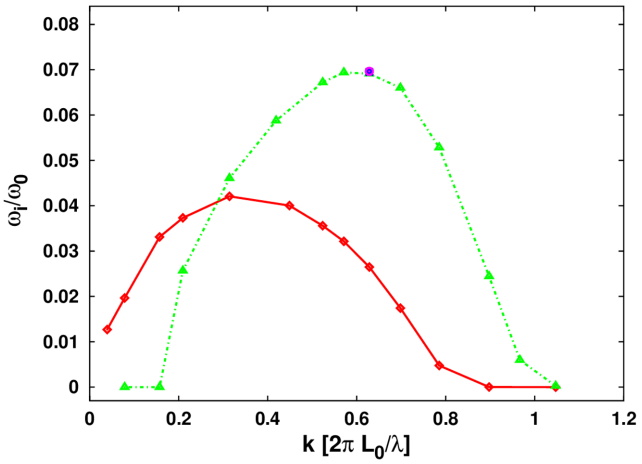

Figure 4. Growth rates of TI (thick red solid line) and DKI (green thick dot–dashed line) modes in the current sheet without guide field. The magenta circle shows the result obtained with doubled numerical resolution.

simulations show a broader dispersion curve, with unstable modes existing beyond $k = 1$ and the peak growth rate $\omega_i/\omega_0 \approx 0.045$, where $\omega_0 = \theta m_e c/eB$, at $k \approx 0.58$ (Cerutti et al. 2014). In our simulations, the peak is more pronounced and located at $k \approx 0.3$. In order to compare our results, we note that with our scaling $\omega_0^{-1} = \theta \mathcal{K}_m = 0.42$ and thus $\omega_i/\omega_0 \approx 0.04$. Overall, we conclude that our results agree quite well with the PIC data.

4.2 Drift-kink instability without guide field

For the study of the DKI, we consider a 2D problem with $\partial_x = 0$. The current sheet is pushed out of equilibrium by perturbing the velocity field of both the electron and positron fluids, $\boldsymbol{U} \rightarrow \boldsymbol{U} + \boldsymbol{u}$, where

$$\boldsymbol{u} = u_0 \cos(kz)\boldsymbol{i}_y\,, \tag{17}$$

with $u_0 = 10^{-3}$. Like in the tearing simulations, the size of the computational domain in the z-direction is set to be exactly one wavelength of the perturbation and we employ relevant periodic boundary conditions at the z boundaries. In the y-direction, we have a comparable size and use the free-flow boundary conditions. The basic parameters of the simulations are given in the Table 2.

The left-hand panel of Fig. 5 illustrates the structure of the unstable modes across the current sheet in our simulations. These results are in a good agreement with the structure of normal modes found in the linear theory of DKI (Zenitani & Hoshino 2007). We quantify the perturbation amplitude using the maximum value of $|u_+^y|$ in the computational box. The right-hand panel of Fig. 5 shows typical examples of its evolution in the simulations.

Fig. 4 shows the dispersion curve. Like in the tearing instability, the dispersion curve of DKI has a clear maximum and in the simulations with longer wavelengths, faster growing parasitic overtone modes can outperform the fundamental mode. In such cases, we compute ω_i only for the initial part of the amplitude curve, where the fundamental mode is still dominant. In order to verify that the numerical resolution is sufficient and the growth rates are trustworthy, we have carried out a separate convergence study. For example,

Table 2. DKI models. The case without guide field.

Name	Resolution	Domain Z	Domain Y	λ	ω_i
KW06	128 × 128	[−3,3]	[−5,5]	6	0.0
KW065	128 × 128	[−3.25,3.25]	[−5,5]	6.5	0.0
KW07	128 × 128	[−3.5,3.5]	[−5,5]	7	0.058
KW08	128 × 128	[−4,4]	[−5,5]	8	0.135
KW09	128 × 128	[−4.5,4.5]	[−5,5]	9	0.159
KW10	128 × 128	[−5,5]	[−5,5]	10	0.165
KW11	128 × 128	[−5.5,5.5]	[−5,5]	11	0.1646
KW12	192 × 128	[−6,6]	[−5,5]	12	0.160
KW15	192 × 128	[−7.5,7.5]	[−5,5]	15	0.137
KW20	256 × 128	[−10,10]	[−5,5]	20	0.110
KW30	384 × 256	[−15,15]	[−10,10]	30	0.061
KW40	512 × 256	[−20,20]	[−10,10]	40	0.0
KW80	1024 × 512	[−40,40]	[−20,20]	80	0.0
KW10h	192 × 192	[−5,5]	[−5,5]	10	0.16553
KW10H	256 × 256	[−5,5]	[−5,5]	10	0.16581

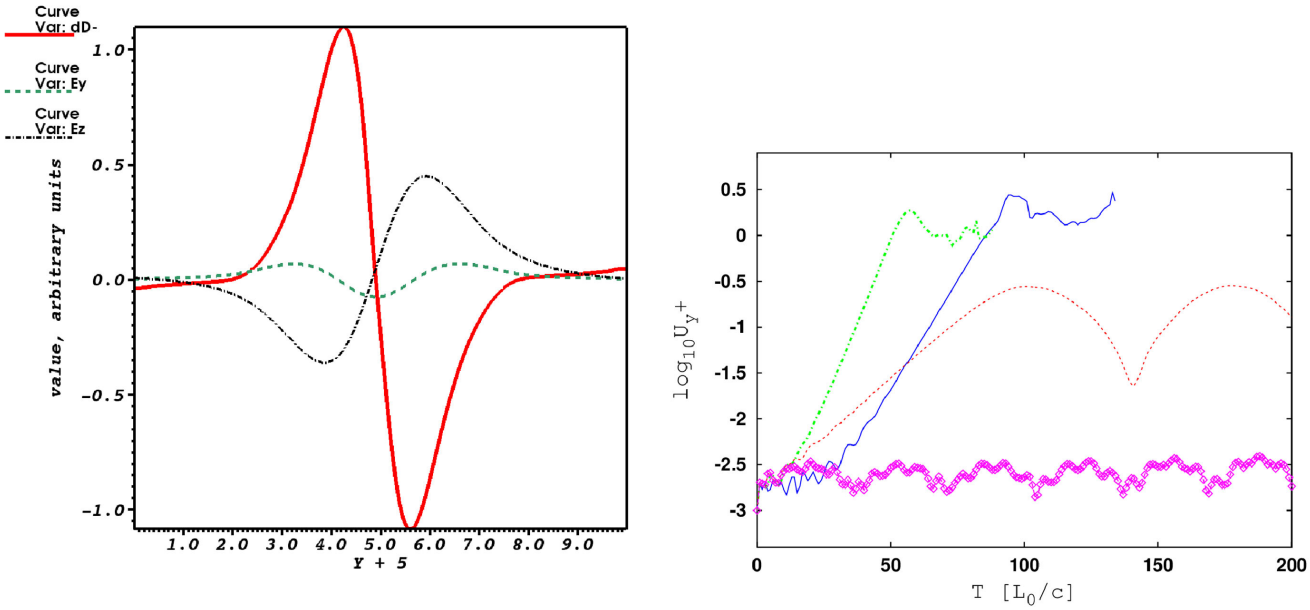

Figure 5. Left-hand panel: structure of DK modes without guide field. The lines show the perturbation of electron density (solid red line), $E_y \times 30$ (dashed green line) and $E_z \times 30$ (dash–dotted black line) as found in the model KW09. The measurements are taken at $t = 66$ along the line $z = 2$. Right-hand panel: growth of DK modes without guide field. The curves represent models KW065 (magenta dashed line with diamonds), KW07 (red dotted line), KW10 (green dot–dashed line) and KW20 (blue solid line). The shown quantity is the maximum value of u_+^y in the computational box.

we repeated the simulations KW10 with higher resolution: 192^2 (model KW10h) and 256^2 (model KW10H). The results indicate that the growth rate error for the model KW10 is below 1 per cent (see Table 2).

Like in the tearing instability, the unstable modes occupy the range $0 < k < 1$, though the long-wavelength modes with $k < 0.2$ appear to be suppressed (see Fig. 4). In the PIC simulations the instability occurs even for $k > 1$ but at a lower growth rate (Zenitani & Hoshino 2007; Cerutti et al. 2014). In our simulations, the growth rate peaks at $k_{\max} \approx 0.6$, where it reaches the value $\omega_{\max} \approx 0.16$. Whereas in the PIC simulations we have $k_{\max} \approx 0.7$ and $\omega_{\max} \approx 0.13$ (Zenitani & Hoshino 2007; Cerutti et al. 2014). Thus, the results of two-fluid and PIC simulations agree with each other quite well again. The linear analysis of Zenitani & Hoshino (2007) shows that the instability domain extends beyond $k = 1$. However this theoretical results is not trustworthy as it is obtained using the long-wavelength approximation, $k \ll 1$.

Interestingly, the short-wavelength modes appear to be non-decaying periodic or quasi-periodic oscillations. The model KW065 is one such example. Its amplitude remains on the level of initial perturbation. The model KW07 seems to be a transitional case, where the initial phase of exponential growth terminates at a relatively low amplitude and is followed by oscillations.

In the PIC simulations, the non-linear phase of DKI is characterized by magnetic dissipation, plasma heating, and widening of the current sheet. All these properties are observed in our simulations as well. Moreover, we find that shock waves develop in electron and positron fluids (see Fig. 6) and they play an important role in plasma heating.

4.3 Current sheets with guide field

Following Zenitani & Hoshino (2008) and Cerutti et al. (2014), we first study the effect of guide field on the fastest growing modes in the case without the guide field. In our study, these are $k \approx 0.31$ ($\lambda = 20$) for TI and $k \approx 0.63$ ($\lambda = 10$) for DKI. The computational domain is $[-5, 5] \times [-5, 5]$ with 128×128 cells for the TI simulations and $[-10, 10] \times [-5, 5]$ with 256×128 cells for the DKI simulations. The strength of the guide field is described by the parameter $\alpha_{\rm gf} = B_z/B_\infty$. The perturbations are introduced in exactly the same way as in the models without the guide field.

The results are shown in Fig. 7. As in the previous studies, the guide field makes a stronger impact on the DKI mode than on the TI mode. For the TI mode, we find that the growth rate is reduced by 50 per cent only at $\alpha_{\rm gf} = 5$, which is in agreement with the two-fluid linear analysis by Zenitani & Hoshino (2008) and their PIC simulations. The PIC simulations by Cerutti et al. (2014) show a somewhat stronger effect, with a 45 per cent reduction already at $\alpha_{\rm gf} = 1$. However, their curve is not monotonic, which may indicate higher numerical errors. As to the DKI mode, we find that it is totally suppressed when $\alpha_{\rm gf} > 1$. This is in a good agreement with the linear stability analysis of Zenitani & Hoshino (2008), who find that for the DKI mode with $k = 0.7$ the critical guide field is $\alpha_{\rm gf,\,c} \approx 0.5$, which also agrees with the results of their PIC simulations. Based on their PIC simulations, Cerutti et al. (2014) find $\alpha_{\rm gf,c} \approx 0.8$ for $k = 0.67$, which is even closer to our results.

Given the strong effect of the guide field on the DKI, we have carried out additional simulations with the aim to clarify the dependence of the DKI dispersion curve on the guide field strength. The parameters of these simulations are given in Table 3 and their results are illustrated in Fig. 7. The surprising result is that the growth rate is not uniformly reduced for all wavelengths. As the guide field increases, the peak of the curve does get lower but in addition the unstable range shifts towards shorter wavelengths. As a result, some modes which grow at $\alpha_{\rm gf} = 0$ become completely stabilized for $\alpha_{\rm gf} \neq 0$ and the other way around (see the right-hand panel of Fig. 7). The blue line in the left-hand panel of Fig. 7 shows the dependence of the maximal growth rate on $\alpha_{\rm gf}$.

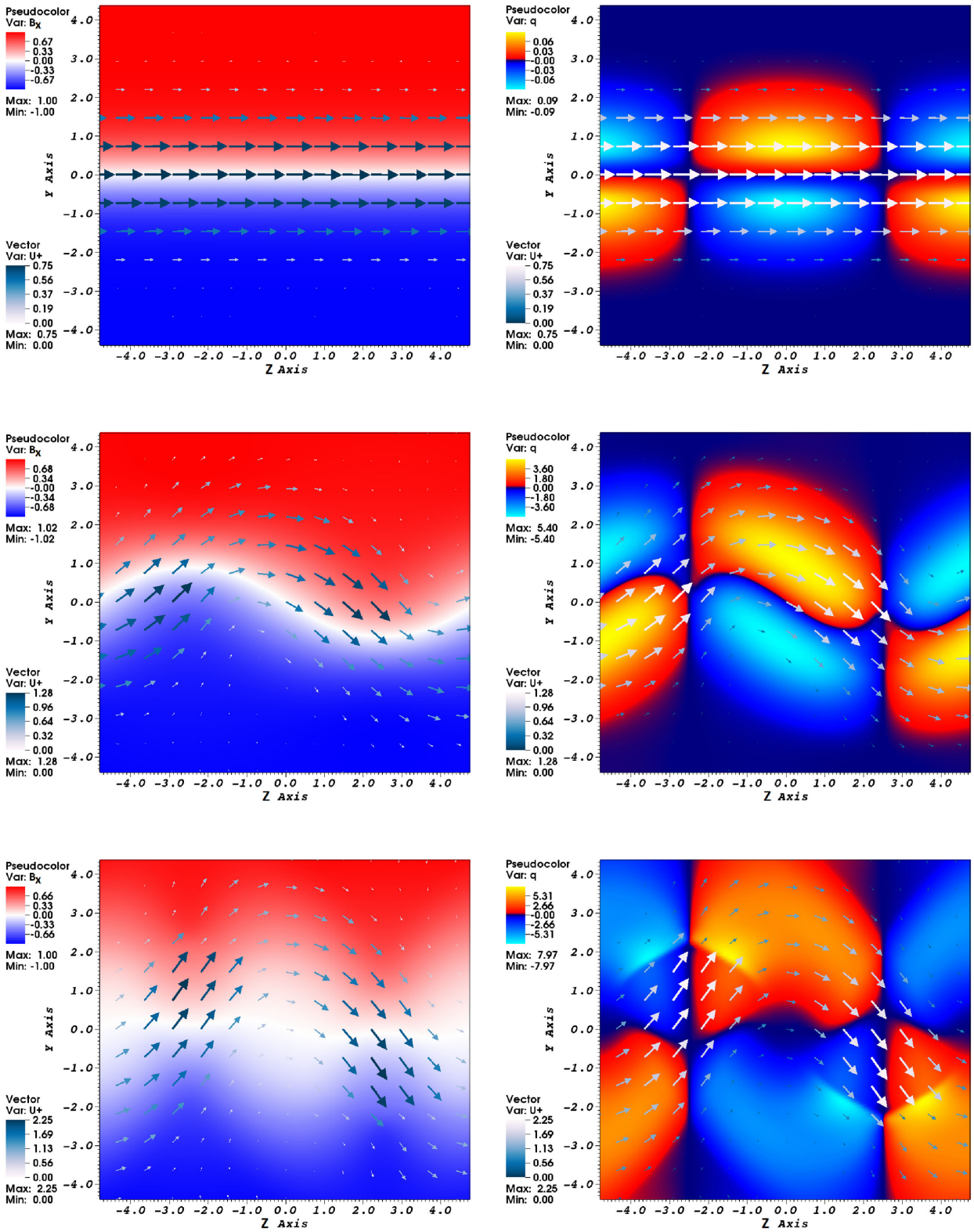

Figure 6. Development of the DKI in the model KW10. In the left-hand panels, the coloured image shows the distribution of the out-of-the-plane component of magnetic field B_x and in the right-hand panels, the distribution of electric charge. The arrows show the velocity field of positrons. The simulation time is $t = 20$, 50 and 58 (from top to bottom). By the time $t = 58$, a significant fraction of magnetic energy has been dissipated and shock waves developed in the electron and positron fluids.

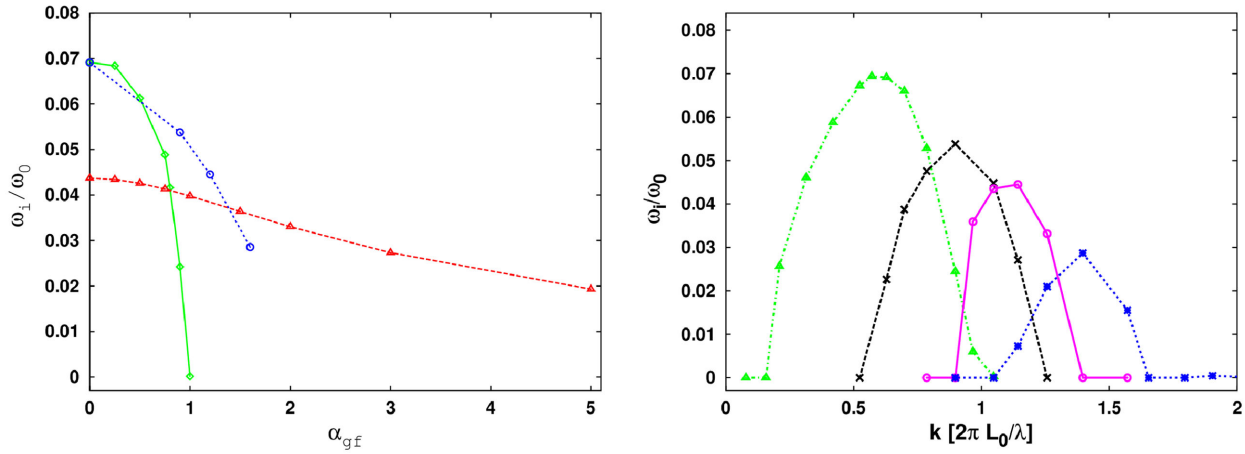

Figure 7. Left-hand panel: dependence of the growth rates of the tearing and DKIs on the strength of guide field, $\alpha_{\rm gf} = B_z/B_\infty$. The red line shows the TI mode with $k \approx 0.3$ ($\lambda = 20$) and the green line the DKI mode with $k \approx 0.6$ ($\lambda = 10$). The blue line shows the growth rate for the fastest growing DKI mode (its wavelength depends on $\alpha_{\rm gf}$). Right-hand panel: growth rates of the DKI in the presence of the guide field. The lines are the dispersion curves for $\alpha_{\rm gf} = 0$ (green triangles), 0.9 (black crosses), 1.2 (magenta squares) and 1.6 (magenta stars).

Table 3. The full set of models with guide field in the study of DKI.

Name	Resolution	Domain Z	Domain Y	λ	$\alpha_{\rm gf}$	ω_i
Ka09W05	192 × 192	[−2.5,2.5]	[−5,5]	5	0.9	0.0
Ka09W055	192 × 192	[−2.75,2.75]	[−5,5]	5.5	0.9	0.064
Ka09W06	192 × 192	[−3.0,3.0]	[−5,5]	6	0.9	0.107
Ka09W07	192 × 192	[−3.5,3.5]	[−5,5]	7	0.9	0.128
Ka09W08	192 × 192	[−4.0,4.0]	[−5,5]	8	0.9	0.113
Ka09W09	192 × 192	[−4.5,4.5]	[−5,5]	9	0.9	0.092
Ka09W10	192 × 192	[−5.0,5.0]	[−5,5]	10	0.9	0.054
Ka09W12	192 × 192	[−6.0,6.0]	[−5,5]	12	0.9	0.0
Ka12W04	192 × 192	[−2.0,2.0]	[−5,5]	4	1.2	0.0
Ka12W045	192 × 192	[−2.25,2.25]	[−5,5]	4.5	1.2	0.0
Ka12W05	192 × 192	[−2.5,2.5]	[−5,5]	5	1.2	0.079
Ka12W055	192 × 192	[−2.75,2.75]	[−5,5]	5.5	1.2	0.106
Ka12W06	192 × 192	[−3.0,3.0]	[−5,5]	6	1.2	0.104
Ka12W065	192 × 192	[−3.25,3.25]	[−5,5]	6.5	1.2	0.086
Ka12W07	192 × 192	[−3.5,3.5]	[−5,5]	7	1.2	0.0
Ka16W038	192 × 192	[−1.9,1.9]	[−5,5]	3.8	1.6	0.0
Ka16W04	192 × 192	[−2.0,2.0]	[−5,5]	4	1.6	0.037
Ka16W045	192 × 192	[−2.25,2.25]	[−5,5]	4.5	1.6	0.068
Ka16W05	192 × 192	[−2.5,2.5]	[−5,5]	5	1.6	0.050
Ka16W055	192 × 192	[−2.75,2.75]	[−5,5]	5.5	1.6	0.017
Ka16W06	192 × 192	[−3.0,3.0]	[−5,5]	6	1.6	0.0

5 CONCLUSION

In this work, we studied the tearing and DKIs of current sheets in collisionless electron–positron plasma by means of 2D two-fluid computer simulations. We set the internal friction (resistivity) to zero and considered current sheets of thickness comparable to the electron skin depth, so that the inertial terms of the generalized Ohm's law become significant. Our results are compared with those of the PIC simulations carried out by other researches for current sheets with similar parameters. We find that there is a good overall agreement between the two-fluid and PIC simulations. In both cases, the fastest growing modes have very similar wavelengths and growth rates when the guide field is small. In both cases, the guide field reduces the growth rates of unstable modes. There are some differences too. For example, the unstable range of both TI and DKI appears to be somewhat narrower and the guide field has a weaker stabilizing effect on the TI mode in the two-fluid simulations. We also find that, in addition to getting lower, the dispersion curve of DKI also shifts towards higher wavenumbers when the guide fields gets stronger. We cannot say if this is in agreement with the PIC simulations due to the lack of relevant PIC data.

It would be naive to hope that the two-fluid simulations could exactly reproduce the results of PIC simulations, and they do not. However, the differences appear to be rather minor. This suggests that the two-fluid model can adequately describe the macroscopic dynamics of plasma with collisionless currents sheets, yielding sufficiently accurate magnetic reconnection rates. In order to confirm this we have started a study of 2D magnetic reconnection in the plasmoid-dominated regime. The preliminary results are encouraging.

ACKNOWLEDGEMENTS

The simulations have been carried out either on a work station with multicore processors or/and on the CFCA cluster (XC30) of National Astronomical Observatory of Japan. We make 2D visualization and analysis using package VISIT (Childs et al. 2012) and OCTAVE. SSK acknowledges support by STFC under the standard grant EP/N023986/1. BMV acknowledge partial support by JSPS (Japan Society for the Promotion of Science): No.2503786, 25610056, 26287056, 26800159. BMV also MEXT (Ministry of Education, Culture, Sports, Science and Technology): No.26105521 and RFBR grant 12-02-01336-a.

REFERENCES

Amano T., Kirk J. G., 2013, ApJ, 770, 18
Barkov M., Komissarov S. S., Korolev V., Zankovich A., 2014, MNRAS, 438, 704
Bessho N., Bhattacharjee A., 2012, ApJ, 750, 129
Bhattacharjee A., Huang Y.-M., Yang H., Rogers B., 2009, Phys. Plasmas, 16, 112102
Biskamp D., 1986, Phys. Fluids, 29, 1520
Cerutti B., Werner G. R., Uzdensky D. A., Begelman M. C., 2014, ApJ, 782, 104
Childs H. et al., 2012, High Performance Visualization–Enabling Extreme-Scale Scientific Insight. p. 357
Dedner A., Kemm F., Kröner D., Munz C.-D., Schnitzer T., Wesenberg M., 2002, J. Chem. Phys., 175, 645
Drenkhahn G., Spruit H. C., 2002, A&A, 391, 1141
Gurovich V. T., Solov'ev L. S., 1986, J. Exp. Theor. Phys., 91, 1144
Kojima Y., Oogi J., 2009, MNRAS, 398, 271
Komissarov S. S., 2007, MNRAS, 382, 995
Komissarov S. S., 2013, MNRAS, 428, 2459
Liu X.-D., Osher S., Chan T., 1994, J. Chem. Phys., 115, 200
Liu Y.-H., Guo F., Daughton W., Li H., Hesse M., 2015, Phys. Rev. Lett., 114, 095002
Loureiro N. F., Schekochihin A. A., Cowley S. C., 2007, Phys. Plasmas, 14, 100703
Lyutikov M., Blandford R., 2003, preprint (astro-ph/0312347)
McKinney J. C., Uzdensky D. A., 2012, MNRAS, 419, 573
Munz C.-D., Omnes P., Schneider R., Sonnendrücker E., Voß U., 2000, J. Chem. Phys., 161, 484
Pétri J., Kirk J. G., 2007, Plasma Phys. Control. Fusion, 49, 1885
Porth O., Komissarov S. S., Keppens R., 2013, MNRAS, 431, L48
Porth O., Komissarov S. S., Keppens R., 2014, MNRAS, 438, 278
Romanova M. M., Lovelace R. V. E., 1992, A&A, 262, 26
Shibata K., Tanuma S., 2001, Earth Planets Space, 53, 473
Shu C.-W., Osher S., 1988, J. Chem. Phys., 77, 439
Sironi L., Spitkovsky A., 2014, ApJ, 783, L21
Uzdensky D. A., Loureiro N. F., Schekochihin A. A., 2010, Phys. Rev. Lett., 105, 235002
Yamaleev N. K., Carpenter M. H., 2009, J. Chem. Phys., 228, 3025
Zelenyi L. M., Krasnoselskikh V. V., 1979, SvA, 23, 460
Zenitani S., Hoshino M., 2001, ApJ, 562, L63
Zenitani S., Hoshino M., 2007, ApJ, 670, 702
Zenitani S., Hoshino M., 2008, ApJ, 677, 530
Zenitani S., Hesse M., Klimas A., 2009a, ApJ, 696, 1385
Zenitani S., Hesse M., Klimas A., 2009b, ApJ, 705, 907
Zhang B., Yan H., 2011, ApJ, 726, 90

This paper has been typeset from a TEX/LATEX file prepared by the author.